Partial retention of radiogenic Pb in galena nanocrystals explains discordance in monazite from Napier Complex (Antarctica)

M.J. Turuani, A.T. Laurent, A.-M. Seydoux-Guillaume, D. Fougerouse, D. Saxey, S.M. Reddy, S.L. Harley, S. Reynaud, W.D.A. Rickard

Partial retention of radiogenic Pb in galena nanocrystals explains discordance in monazite from Napier Complex (Antarctica)

Turuani M.J.[1*], Laurent A.T.[1], Seydoux-Guillaume A.-M.[1], Fougerouse D.[2,3], Saxey D.[3], Reddy S.M.[2,3], Harley S.L.[4], Reynaud S.[5], Rickard W.D.A.[3]

[1]Univ Lyon, UJM, UCBL, ENSL, CNRS, LGL-TPE, F-42023, Saint Etienne, France

[2]School of Earth and Planetary Sciences, Curtin University, Perth, Western Australia 6845, Australia

[3]Geoscience Atom Probe, John de Laeter Centre, Curtin University, Perth, Western Australia 6845, Australia

[4]School of Geosciences, University of Edinburgh, Edinburgh EH9 3FE, UK

[5]Univ Lyon, Université Jean Monnet, CNRS 5516, IOGS, Laboratoire Hubert Curien, F 42000 Saint-Étienne, France

ABSTRACT

The discordance of U–Th–Pb isotopic systems in geochronometers, and how such data are interpreted, are still major issues in the geosciences. To better understand the disturbance of isotopic systems, and how this impacts the derivation of geologically-meaningful ages, previously studied discordant monazite from the ultrahigh temperature paragneiss of the Archean Napier Complex (Antarctica) have been investigated. Monazite grains were characterized from the micro to the nanoscale using an analytical workflow comprising laser ablation inductively coupled plasma mass spectrometry (LA-ICP-MS), secondary-ion mass spectrometry (SIMS), electron microprobe (EMP), transmission electron microscopy (TEM) and atom probe tomography (APT). Results reveal that the least discordant monazite, hosted in

garnet and rutilated quartz, contain a large number of small Pb-bearing nanominerals (Ø ~ 50 nm) while the most discordant monazite, hosted in the quartzo-feldspathic matrix, contain a smaller number of Pb-bearing nanominerals bigger in size (Ø ~ 50 to 500 nm). The degree of the discordance, which was previously correlated with textural position is mechanistically related to the partial retention of radiogenic Pb (Pb^*) in distinct Pb^*-bearing nanominerals (e.g. PbS) within the monazite grains. *In-situ* dating (U–Pb systems with LA-ICP-MS and SIMS), and isotopic information obtained by using APT ($^{207}Pb/^{206}Pb$ isotopic signature of galena and $^{208}Pb/^{232}Th$ ages of the monazite matrix) allow the timing of Pb-disturbance and mobility to be constrained. Results show that monazite grains crystallized at *ca.* 2.44 Ga and were affected by two episodes of Pb^* mobility. The first episode (t_1) at *ca.* 1.05 Ga, led to crystallization of a first generation of Pb^*-bearing nanominerals and a complete resetting of the monazite matrix at the nanoscale. The second episode (t_2) at *ca.* 0.55 Ga was associated with the crystallization of a second generation of Pb^*-bearing nanominerals with a $^{207}Pb/^{206}Pb$ signature indicating a mixing of two Pb^* components: a component from the monazite matrix and remobilized Pb^* from the first generation of Pb^*-bearing nanominerals. This second event is characterized by a more localized resetting of the monazite matrix at the nanoscale compared to the t_1 event. These results indicate the potential of nanoscale studies of Pb-rich nanominerals within monazite to yield important details of the themal history of complex metamorphic terranes.

Keywords: U–Th–Pb discordance – monazite – Pb mobility – nanogeochronology- atom probe tomography

1. INTRODUCTION

Accessory mineral U–Th–Pb geochronology is widely used in Earth Sciences because the existence of two U–Pb and one Th–Pb decay chains, each with different half-lives, allows direct evaluation of isotopic disturbance and the accuracy of calculated dates. If the dates calculated

from the three decay chains differ, then the system under consideration is referred to as discordant. Discordance is common in ancient and polymetamorphic rocks, where it typically indicates Pb mobility or loss, and if not recognized may lead to erroneous conclusions with respect to the geological history (Corfu, 2013). In situations where only one event is responsible for Pb mobility, the time of Pb disturbance may be deduced by regression of discordant isotopic data on graphs of $^{206}Pb/^{238}U$ vs $^{207}Pb/^{235}U$ or $^{207}Pb/^{235}U$ vs $^{208}Pb/^{232}Th$ (Allègre et al., 1974; Tera and Wasserburg, 1972; Wetherill, 1963). However, multiple episodes of Pb disturbance result in more complex data distributions that may be difficult to identify and reliably interpret (Gebauer and Grünenfelder, 1979). This is particularly the case when the scale or mechanism of Pb mobility differs between events. However, assessing the scale of Pb mobility as well as the mechanisms by which Pb is disturbed, is typically difficult. The nanoscale quantification of Pb distribution, coupled with isotopic analysis, has the potential to provide constraints on the causes and scales of Pb mobility to yield a unique insight into the nature of discordance in the U–Th–Pb isotopic systems (Peterman et al., 2016; Valley et al., 2014).

Fine-scale characterization of the location and behaviour of the radiogenic daughter element (Pb^*) in host minerals relies on the correlation of structural observations with isotopic measurements at the nanoscale. Transmission electron microscopy (TEM) has revealed Pb-rich nanominerals in discordant zircon, either as native Pb (Kusiak et al., 2015) or Pb-oxide (Kusiak et al., 2019). Similar features have been reported in discordant monazite (Seydoux-Guillaume et al., 2003) and phase separation of Pb-enriched domains in monazite have been identified through the integration of TEM and atom probe tomography (APT) analyses (Seydoux-Guillaume et al., 2019). The isotopic compositions of such heterogeneities for U–Th–Pb geochronometers such as zircon, monazite and rutile have been quantified using APT (Arcuri et al., 2020; Blum et al., 2018; Fougerouse et al., 2021a, 2021b, 2018; Peterman et al., 2016; Seydoux-Guillaume et al., 2019; Valley et al., 2015, 2014; Verberne et al., 2020). These studies

typically use an advanced analytical workflow to constrain the scale of Pb mobility and the timing of isolation of Pb from parental U and Th (Peterman et al., 2016; Seydoux-Guillaume et al., 2019; Valley et al., 2015). This approach, which integrates textural, microstructural, compositional and isotopic analyses from the micro- to the nanoscale yields significant advances on the causes of isotopic discordance and ages variation at the microscale (Peterman et al., 2016; Seydoux-Guillaume et al., 2018a).

Studies on natural zircon have demonstrated that isotopic discordance may be caused by Pb^* mobility associated with the annealing of radiation damage during high temperature metamorphic conditions, resulting in isolated Pb^* reservoirs (Kusiak et al., 2019, 2015; Peterman et al., 2021, 2016; Whitehouse et al., 2017). In contrast, monazite is less sensitive to the thermal history of the host rock since natural monazite remains crystalline thanks to a defect recovery mechanism operating event at moderate temperature (> 180 °C; Seydoux-Guillaume et al. 2018b). Pb^* mobility in monazite from micro to nanoscale is promoted by fluid-assisted mechanisms, such as a coupled dissolution-precipitation process (Grand'Homme et al., 2018; Seydoux-Guillaume et al., 2002), and by deformation-assisted mechanisms both in fluid-present (Wawrzenitz et al. 2012) and fluid-absent environments (Erickson et al., 2015; Fougerouse et al., 2021b). As a result, the effects and interplay of such mechanisms, on the formation and nature of nanoscale Pb^* heterogeneities as well as their impact on discordance in monazite cannot simply be derived from our knowledge of zircon.

This study re-investigates discordant monazite grains reported by Black et al. (1984) from an Archean polymetamorphic granulite of the Napier Complex, East Antarctica. Multiple advanced micro- to nanoscale analytical techniques are used to provide unique constraints on the development and evolution of discrete Pb^* reservoirs within variably-discordant monazite. The integration of isotopic analyses over a range of scales is critically evaluated within the

context of a well-constrained metamorphic history to provide unique constraints on the nanoscale mechanisms accommodating two stages of Pb-disturbance.

2. METHODS

Microscale imaging of monazite was conducted at 20 keV with field emission gun scanning electron microscopy FEG-SEM Zeiss supra 55vp. The instrument is also equipped with an energy dispersive X-ray (EDX) spectrometer.

Uranium–Th–Pb isotopic analyses by LA– ICP–MS were performed at the Laboratoire Magmas et Volcans (Clermont-Ferrand, France). The laser ablation systems consist of a Resonetics Resolution M-50E system equipped with an ultrashort pulse ATL excimer 193 nm laser coupled to an Agilent 7500 cs ICP–MS. A Laser spot diameter of 9 µm was used with 1 Hz repetition rate and a fluence of 7.5 J/cm^2. The ^{204}(Pb+Hg) signal was monitored but no common-Pb correction was applied. Analytical procedures and reproducibility are reported in detail in Appendix A. SIMS was undertaken on a CAMECA IMS 7f-Geo hosted at the NERC Ion Micro-Probe Facility, School of Geosciences, Edinburgh University (UK), under conditions detailed in Appendix A. The technique was specifically employed to search for the presence of any ^{204}Pb (common Pb; Pb_c) because LA-ICP-MS cannot be employed due to the unresolvable isobaric interference between ^{204}Pb (203.9730), and ^{204}Hg (203.9735). With the SIMS technique there is a potential isobaric interference from the molecular species $[^{232}Th^{144}Nd^{16}O_2]^{2+}$ (mass 407.9379, M/z = 203.9690). This interference can be resolved by correlating $[^{232}Th^{144}Nd^{16}O_2]^{2+}$ counts per second (cps) with $^{143}Nd^{31}P^{16}O_2$ (205.87) in the 5037 monazite sample and comparing this to Moacyr reference material data, which shows that these data follow a linear correlation (more details in Appendix A). SIMS analyses reported a maximum of 0.06 cps associated with ^{204}Pb estimated in Moacyr reference material. As the counts of mass 204 in sample 5037 monazite are less than, or overlap, those for Moacyr (2.8

cps and 3.7 cps respectively; Appendix C), the figure of 0.06 cps for ^{204}Pb is applied as a maximum correction for common Pb on ^{206}Pb, ^{207}Pb and ^{208}Pb in sample 5037 monazite. Age data from SIMS have higher uncertainties than those from LA-ICP-MS as the SIMS methodology was optimized to assess Pb_c and not to obtain high-precision dates. U–Th–Pb EMP dating was conducted using a CAMECA SXFive at the Microcharacterization Center Raimond Castaing, at Toulouse (France). The analytical conditions were 15 keV and 200-300 nA, following the protocol outlined in Laurent et al. (2016), and are detailed along with age reproducibility in Appendix A.

Nanoscale characterization by TEM and scanning transmission electron microscopy (STEM) were performed with a Cs-corrected NeoARM200F Cold FEG TEM operated at 200 keV, owned by the Consortium Lyon Saint-Etienne de Microscopie (FED 4092) and hosted within the Hubert Curien Laboratory, Saint-Etienne (France). APT data were collected using a CAMECA Local Electrode Atom Probe LEAP 4000X HR hosted at the Geoscience Atom Probe Facility at Curtin University, Perth (Australia). APT data were collected using a UV laser (λ = 355 nm) pulsed at 125 kHz and 30-300 pJ (details in Appendix A). In the APT mass spectra, peaks at least twice higher than the background level were identified and reconstructed in 3 dimensions. For monazite, voltage evolution reconstructions were utilized with an evaporation field of 27.02 V/nm^2 and an atomic volume of 0.01245 nm^3 (Fougerouse et al., 2021c). TEM samples were prepared using a with a Thermo Fisher Scientific FEI Helios Nanolab 600i focused-ion beam scanning electron microscope (FIB/SEM) hosted by MANUTECH USD platform, at Hubert Curien laboratory, Saint-Etienne (France). A Tescan Lyra3 Ga^+ FIB-SEM housed at Curtin University was used for preparation on needle-shaped APT specimens. More details on instrument, analytical conditions and data processing are provided in Appendix A.

Isotopic dates from the APT data were calculated using $^{208}Pb/^{232}Th$ ratios measured on $^{208}Pb^{2+}$ and $^{232}ThO^{2+}$ peaks, following the correction procedures of (Fougerouse et al., 2020;

see Appendix A for details). $^{207}Pb/^{206}Pb$ ratios were estimated from APT data on galena inclusions using $^{207}Pb^{2+}$ and $^{206}Pb^{2+}$ peaks and following the methodology of Blum et al., (2018) to correct the effect on the thermal peak of $^{206}Pb^{2+}$ on $^{207}Pb^{2+}$ peak (see Appendix A for details).

3. GEOLOGICAL CONTEXT AND SAMPLE DESCRIPTION

The studied monazite grains are from an Archean granulite (sample 5037; Black et al., 1984) collected at Zircon Point in the Napier Complex, East Antarctica (Fig. 1A, B). The granulite is a garnet-rich migmatized paragneiss preserving a well-developed, high-grade, layer-parallel fabric composed of rutilated quartz (Rt-quartz) ribbons, mesoperthitic feldspar, sillimanite and elongated poikiloblastic garnet (Appendix B.1, S_1, S_2; Black et al., 1983, 1984). This mineral paragenesis corresponds to a major late-Archaean ultrahigh temperature (UHT) event (1050 – 1120°C, 7-11 kbar) at *ca.* 2.58 – 2.48 Ga (Harley and Motoyoshi, 2000; Hokada et al., 2004 Kelly and Harley, 2005).

The sample is affected by retrogression involving the development of secondary biotite within fractures in garnet (Appendix B.1, S_3; Black et al. 1983), exsolution of perthitic feldspar and the recrystallization of the quartzo-feldspathic matrix as fine-grained granoblastic aggregates containing rutile-free quartz (Appendix B.1; Black et al., 1983). This retrogressive episode in the southern Napier Complex area, including Zircon Point, corresponds to amphibolite-facies conditions and is associated with localized shearing and pegmatite intrusions. This event overprints the Napier Complex, especially in Casey Bay and is temporally constrained by ID-TIMS U–Pb zircon and monazite discordant fractions from paragneiss at 1073 Ma and 1087 ± 29 Ma (zircon from McIntyre Island; Black et al., 1983, monazite from Zircon Point; Black et al., 1984, Fig. 1B) as well as by a Pb-total age on monazite from a pegmatite at 1094 ± 67 Ma (Zircon Point; Asami et al., 2002). Hence, this lower-grade event has been linked to the Rayner Structural Episode, which took place in the Rayner Complex at

amphibolite- to granulite-facies conditions around 1000 – 900 Ma ago (Black et al., 1987; Harley and Hensen, 1990; Harley, 2003; Sheraton et al., 1980). At *ca.* 500-550 Ma, hydrothermal activity is reported in the Napier Complex (Carson et al., 2002) and intrusion of pegmatites in the nearby Ayatollah Island (Fig. 1B) is recorded by a Rb–Sr age on a pegmatite at 522 ± 10 (2σ) Ma. These events reflect renewed magmatic and hydrothermal activity at Zircon Point (Black et al., 1983).

Monazite grains are hosted in garnet, sillimanite, Rt-quartz or along grain boundaries in the S_2 or recrystallized S_3 quartzo-feldspathic matrix. Previous petrographic and isotopic work (isotope dilution thermal ionization mass spectrometry ID-TIMS on multigrain separates) on monazite from sample 5037 identified three optically-distinct colour groups that were correlated with the monazite host mineral and recorded three distinct, discordant isotopic compositions (Fig. 1C; Black et al., 1984). The three groups define a discordant line (mean square weighted deviation - MSWD = 11), with upper and lower intercepts at 2429 ± 17 (2σ) Ma and 1087 ± 29 (2σ) Ma respectively (Fig. 1C). Chemical compositions were reported to be similar for the three monazite groups, and TEM investigations did not show differences in crystallinity (Black et al., 1984). Brown monazite, hosted either in garnet or Rt-quartz, were < 30% discordant whereas clear monazite (yellow and grey), hosted in the quartzo-feldspathic matrix, were found to be at least 50% discordant (Fig. 1C). This unique pattern of discordance was tentatively explained in term of variable Pb loss with the three groups reflecting the differing capacities of their host mineral to shield the monazite crystals from late, post-metamorphic fluids (Black et al., 1984).

4. MONAZITE CHARACTERIZATION

A microscale analytical survey of 35 *in-situ* monazite grains was complemented by nanoscale characterization of a subset of these monazite crystals (Mnz2, Mnz4, Mnz17, Mnz25;

Fig.2, Appendix B.2) according to their textural position (host mineral). A single TEM foil was prepared from a monazite grain hosted in both Rt-quartz (Mnz17; Fig. 2A) and garnet (Mnz4; Appendix B.2) and three TEM foils were prepared from a monazite grain located in the quartzo-feldspathic matrix (Mnz25; Fig. 2B). Fourteen needle-shaped atom probe specimens were prepared from Rt-quartz hosted monazite (Mnz17; Fig. 2A) and quartzo-feldspathic matrix hosted monazite (Mnz25 and Mnz2; Fig. 2B, C). Specimen locations are shown in Fig. 2A, C, F.

4.1. Microscale to nanoscale features

Monazite crystals display complex textural features in greyscale back-scattered electron (BSE) images (Fig. 2). These include a core-rim texture, highlighted generally by dark cores (Fig. 2A-C), bright (Th-rich) linear features traversing the core (Fig. 2B, Appendix B.2), zonation (Fig. 2A) or overgrowths (Appendix B.2). These different textures are present in monazite grains from different hosts but are not systematically present in all grains. Monazite located in the quartzo-feldspathic matrix are range between 50-250 µm in size while monazite in garnet or Rt-quartz are range between 20-80 µm in size. Sub-micrometer (Ø < 1µm) dark (low-BSE coefficient) circular spots are present in all monazite grains, as are sub-micrometer (Ø < 1 µm), bright (high-BSE coefficient) circular spots (Fig. 2D-F, Appendix B.2). Bright spots are larger in monazite hosted in the quartzo-feldspathic matrix than those hosted in Rt-quartz or garnet (Fig. 2D-F). They are also more abundant and larger in the rim of Mnz25 than in the core (Fig. 2E).

At the nanoscale the bright spots correspond to distinct crystalline Pb-bearing minerals (lightest nanoscale features on STEM images; Fig. 3) and are often spatially associated with a dark silicate and amorphous material (Fig. 3). Individual Pb-bearing minerals and amorphous silicate material also exist. The distribution and the size of these Pb-bearing minerals varies

within the grain (e.g. core versus rim) and with the textural position of the monazite grain. Monazite grains in Rt-quartz and garnet have a large number of Pb-bearing minerals (Ø < 50 nm; Fig. 3A, Appendix B.3) compared to grains within the quartzo-feldspathic matrix (Ø > 50 nm; Fig. 3B, C). In monazite grains from the quartzo-feldspathic matrix, Pb-bearing minerals are also more abundant and smaller in the rim (Ø < 100 nm; Fig. 3B), than in the core (Ø > 100 nm; Fig. 3C).

Two of the largest Pb-bearing minerals (Ø ~ 1 µm) have been analyzed by APT. These minerals comprise Pb and S, (Fig. 4) and are devoid of U or Th (Fig. 4B). Compositions estimated from the APT data (S = 47.76 ± 0.02 at % and Pb = 52.18 ± 0.02 at % and S = 48.79 ± 0.06 at % and Pb = 50.60 ± 0.06 at %; Appendix B.6) are consistent with the stoichiometry of galena. Electron diffraction patterns acquired by TEM on a similar Pb-bearing mineral (Ø ~ 500 nm) are compatible with these minerals being galena (Appendix B.4).

4.2.Isotopic data and geochronology

The corrected $^{206}Pb/^{204}Pb$ ratios obtained with SIMS are on average, 44284 for sample 5037 monazite and 9225 for Moacyr reference material. In each case the amount of common ^{206}Pb ($^{206}Pb_c$), is significantly less than 1% of total ^{206}Pb (0.038% for sample 5037 and 0.189% for Moacyr). Thus, monazite crystals contain negligible ^{204}Pb indicating that Pb_c can be discounted as a contaminant in the LA-ICP-MS results and as a contributor to the Pb present in the galena grains.

The analytical volume of the different geochronological approaches applied to the monazite grains range over nine orders of magnitude. Dates from LA-ICP-MS (Appendix D), SIMS (Appendix C) and EMP (Appendix E) techniques range between 2435 ± 150 Ma (2σ) Ma and 874 ± 28 Ma (2σ) and are independent of the chosen chronometer ($^{206}Pb/^{238}U$, $^{208}Pb/^{232}Th$; Fig. 5, Appendix F). $^{208}Pb/^{232}Th$ dates from APT data tend towards the lower end of this spectrum,

whilst ID-TIMS on multiple grains (Black et al. 1984) tend towards the oldest dates (Fig. 5). Moreover, at the scale of the population, the spread of monazite dates is systematically related to where the monazite is hosted and not to its Th/U ratio nor to the analysis location with respect to core and rim (Fig. 5, Appendix G.1-4).

U–Pb isotopic data gathered *in-situ* by LA-ICP-MS and SIMS are discordant and spread along a discordia line, D_{all}, defined by an upper intercept of 2383 ± 36 Ma (2σ) and a lower intercept of 931 ± 45 Ma (2σ) (MSWD = 4.7; Fig. 6A). U–Pb and Th–Pb systems are also discordant (Appendix G.5). The data from monazite grains hosted in Rt-quartz and garnet plot close to the upper intercept of the discordia line and show less than 50% Pb-loss. These data alone yield an upper and a lower intercept of 2440 ± 39 Ma (2σ) and 1045 ± 132 Ma (2σ) respectively (MSWD = 0.84, discordia D_{IM}; Fig. 6A, Appendix G.6). In contrast, the monazite grains hosted in the quartzo-feldspathic matrix record up to 90% Pb-loss (Fig. 6A).

LA-ICP-MS and SIMS U–Pb data from monazite grains hosted in the quartzo-feldspathic matrix (Mnz2 and Mnz25; Fig. 3B, C) define two distinct discordia trends when ranged by galena-rich rim or galena-poor core region (Fig. 6B) and also related locally to the Th/U ratio of the analytical spots (Appendix G.7). The discordia D_{LI} from the galena-rich rim region (yellow symbols, MSWD = 2), yields upper and lower intercepts at 2434 ± 181 Ma (2σ) and 1049 ± 248 Ma (2σ) respectively, and intersect the $^{207}Pb/^{206}Pb$ axis at $(^{207}Pb/^{206}Pb)_{DLI}$ = 0.21 ± 0.03 (2σ). Data from the galena-poor core region (blue symbols) form a discordia D_{FI} (MSWD = 2.6) which intersects the $^{207}Pb/^{206}Pb$ axis at $(^{207}Pb/^{206}Pb)_{DFI}$ = 0.16 ± 0.03 (2σ) and has upper and lower intercepts with concordia at 2120 ± 207 Ma (2σ) and 631 ± 224 Ma (2σ) respectively. By fixing the upper intercept at 2440 Ma for the sparse galena domain data, the lower intercept is at 861 ± 58 Ma (2σ) (discordia D_{fix}, MSWD = 4).

APT-derived $^{208}Pb/^{232}Th$ dates from monazite grains hosted in the quartzo-feldspathic matrix (Mnz25 and Mnz2) and the Rt-quartz (Mnz17) are calculated from areas that do not

contain galena (Fig. 7, Appendix H, APT mass spectrum Appendix B.5). $^{208}Pb/^{232}Th$ dates range between 1188 ± 202 Ma (2σ) and 712 ± 121 Ma (2σ) (Fig. 5, Appendix G.8) and statistically correspond to a single date population (MSWD = 0.72; Appendix G.8-9). Using the complete dataset, the mean $^{208}Pb/^{232}Th$ ratio is 0.0518 ± 0.0137 (2σ) corresponding to a date of 1021 ± 263 Ma (2σ). The $^{208}Pb/^{232}Th$ mean for specimens obtained from the rim of Mnz25 and Mnz2 is 0.0540 ± 0.0107 (2σ) yielding a date of 1063 ± 205 Ma (2σ) (MSWD = 0.34) while the mean $^{208}Pb/^{232}Th$ for core specimens from the same grains is 0.0497 ± 0.0156 (2σ) corresponding to 979 ± 301 Ma (2σ) (MSWD = 1.04; Appendix G.8).

APT-derived $^{207}Pb/^{206}Pb$ ratios from the two analysed galena (Gn 1 and Gn 2; Fig. 4) are 0.20 ± 0.02 (1σ) and 0.150 ± 0.003 (1σ) respectively. The APT data show no peaks associated with ^{204}Pb (Fig. 4C).

5. DISCUSSION

5.1. Interpretation of microscale age pattern

Isotopic analyses of Pb by SIMS in selected grains did not show any ^{204}Pb component in the time resolved signal, which is interpreted as the absence of significant "common"-Pb in the microscale analyses. Consequently, all the Pb present in monazite and galena is interpreted to be of radiogenic origin and is derived from within the monazite.

Considering the whole dataset (n = 89), the discordia D_{all} MSWD (4.7) indicates that the dispersion of the data cannot result from a single population (i.e. a single disturbing event) at 95% confidence level (Wendt and Carl, 1991). In contrast, the D_{IM} discordia derived from monazite hosted in Rt-quartz and garnet yields an acceptable MSWD of 0.84 compatible with a single disturbing event and is thus the most robust to derive monazite crystallization age (t_0) at 2440 ± 39 Ma (Fig. 6A). This age is identical within errors to previous upper intercept ages calculated with ID-TIMS data on monazite and zircon grains from Casey Bay (Fig. 1C; Black

et al., 1984, 1983) and to 2451 ± 15 Ma zircons in equilibrium with garnet from Crosby Nunataks in Amundsen Bay (Fig. 1A; Taylor et al., 2017). Even if *in-situ* isotopic dating on zircon may present slightly older ages than obtained in monazite (e.g. Hokada et al., 2004; Kelly and Harley, 2005), monazite are truly and fully included in garnet implying garnet growth and/or recrystallization through to that age, extending the timescale of the UHT to HT metamorphism even further. Thus, the monazite age of 2440 ± 39 Ma provides a lower limit for the UHT metamorphism in this part of the Napier Complex. The lower intercept t_1 of the D_{IM} discordia (1045 ± 132 Ma) is within error of the Rayner Complex event and reflects the time of U–Th–Pb chronometer disturbance. This is confirmed by the $^{208}Pb/^{232}Th$ average age of 1021 ± 263 Ma (2σ) derived by APT analysis of galena-free monazite that points to a complete resetting of the monazite matrix during the Rayner Complex tectonothermal event.

The monazite grains (Mnz25 and Mnz2) hosted in the quarzto-feldspathic matrix show two discordia trends (yellow and blue symbols, Fig. 6B). D_{LI} discordia is defined by the galena-rich rim and is consistent with the D_{IM} discordia. D_{FI} is defined by the galena-poor core, corresponding to areas which have undergone 70 – 90 % Pb^* loss at t_1, and suggests a younger disturbing event, defined by the lower intercept at t_2 = 631 ± 224 Ma (2σ) (Fig. 6B). This age lies within uncertainty of the timing of pegmatite intrusions within the Napier Complex at Casey Bay at *ca.* 530 Ma (Carson et al., 2002; Black et al., 1983), so may correspond with this hydrothermal activity (t_2).

5.2. Origin of discordance revealed at nanoscale

Black et al. (1984) highlighted that the least discordant monazite fraction was brown in color, whereas the most discordant was clear (grey and yellow). Our microscale data confirm a similar systematic relationship between monazite color and the percentage of Pb-loss. In addition, SEM and TEM investigations revealed that the color relates to the density of galena

inclusions, with monazite showing the highest density of galena being brown in color, whilst the clearest monazite grains contain a lower density of galena inclusions (Fig. 3, 5, 6).

Considering the microscale U–Th–Pb data, the dates of monazite hosted in the quartzo-feldspathic matrix, tend toward the lower intercept t_1 (80 % Pb-loss ; Fig. 5) whereas the dates from monazite hosted in Rt-quartz and garnet tend toward the upper intercept (t_0) implying only limited Pb^* loss (10-50 %) at the grain scale . This difference is again explained by the large amount of galena, homogeneously distributed considering a micrometric analytical volume, in Rt-quartz hosted monazite compared to monazite hosted in the quartzo-feldspathic matrix (Fig. 3A) Thus, the discordia (D_{IM}) is interpreted as a mixing pattern between galena and monazite host, representing two different reservoirs of Pb^* derived from the monazite itself. A similar pattern is observed within individual grains (e.g. Mnz25), where core regions with a smaller number of galena show a higher percentage of Pb-loss than the galena-rich rim (Fig. 6B).

The ability of monazite to retain galena crystals and thereby much of the Pb^* is partly related to their textural position; monazite crystals hosted in Rt-quartz and garnet retain more Pb^* in the form of galena than monazite crystals hosted in the quartzo-feldspathic matrix (Fig. 3, 5, 6A). High retention of Pb^* is associated with a small galena size (< 50 nm), and a more homogenous distribution through the crystal (Fig. 3). This property could be related to fluids access to monazite. Rt-quartz and garnet, which are anhydrous UHT phases, could limit the quantity of fluids which are thus rapidly saturated in Pb, inducing a short-range (re)precipitation of Pb-bearing nanominerals within the grain. In contrast, a larger quantity of fluids might access monazite hosted in quartzo-feldspathic matrix implying a more efficient leaching of Pb^* which is then lost from the grain. Shielding of monazite by its host-mineral, also observed at other UHT localities (e.g. Paquette et al., 2004; Madagascar), does not act as the trigger for the development of the Pb-bearing minerals within monazite but is instrumental to their preferential

preservation and retention. Further studies will be undertaken to characterize the mineralogical variety of the Pb-bearing nanominerals present in monazite grains.

To summarize, the difference in color is interpreted to relate to the amount and distribution of galena crystals within the different monazite grains, which in turn is related to the percentage of Pb-loss. The inverse correlation between the percentage of Pb-loss and the amount of galena (Fig. 3, 5, 6) reflects partial retention of radiogenic Pb^{*} at the grain scale through the crystallization of galena. The volume analyzed with micro-scale dating methods (ID-TIMS, LA-ICP-MS, SIMS and EMP) therefore corresponds to a mixing between monazite and galena preserving distinct isotopic composition. The retention of galena is promoted by monazite shielding in (anhydrous) UHT phases like garnet and Rt-quartz.

The largest Pb-bearing nanominerals observed in this study have been identified as galena (PbS). Crystallization of galena requires Pb but also S which may be derived either from an external source such as metamorphic fluids or from the monazite itself. Sulphur incorporation in the monazite lattice occurs mostly through the clino-anhydrite substitution $Ca^{2+} + S^{6+} = REE^{3+} + P^{5+}$ (Chakhmouradian and Mitchell, 1999), although other studies suggest more complex substitutions involving S^{2-} and S^{4+} (Broom-Fendley et al., 2020). The presence of S-rich monazite in metamorphic rocks is well-documented, including in UHT granulite (Laurent et al., 2016). Under low-grade metamorphic conditions (greenschist facies), S incorporation in monazite is typically associated with high common Pb content and ore precipitation in the host rock (Krenn et al., 2011; Pršek et al., 2010; Suzuki and Kato, 2008). Under high-grade conditions, S-rich monazite reflects Fe-sulphide breakdown under oxidizing conditions and have been reported to contain negligible common Pb (Laurent et al., 2016). Since common Pb is negligible in monazite and galena from the present study, sulfur could be derived from the monazite itself rather than from an external source. The presence of sulfur in high-grade monazite could thus contribute heavily to the preservation of Pb^{*} as galena nanocrystals.

5.3. Galena Pb isotopic signatures

Historically, discordance issues have been resolved by lowering the analytical volume until homogenous Pb^* isotope reservoirs can be analyzed separately (i.e. galena and monazite matrix). As there is no U or Th in the galena, their measured $^{207}Pb/^{206}Pb$ ratios have not evolved since their growth. As SIMS results support that common-Pb contamination of the monazite is negligible, the $^{207}Pb/^{206}Pb$ ratio of the galena records the Pb^* composition of the monazite when the galena crystallised. Since the monazite crystallisation age is known, then the $^{207}Pb/^{206}Pb$ of galena can be used to estimate the time of Pb^* isolation from U and Th in the host monazite, which corresponds to the time of galena growth. The evolution of the Pb isotopic ratio of the monazite is constrained by the geological history highlighted in the previous sections and thus bounded by the *ca.* 2440 Ma (t_0), 1045 Ma (t_1), and 550 Ma (t_2) geological events (Fig. 8C). This assumption is confirmed by the scatter of microbeam analyses that fall in a triangle bounded by ca. 2.44 Ga, 1.05 Ga and 0.55 Ga in the Tera-Wasserburg plot (Fig. 6).

The $^{207}Pb/^{206}Pb$ ratio measured in Gn 1 is best explained by Pb^* isolation at 1045 Ma from a monazite that crystallized at 2440 Ma, which would correspond to a theoretical $^{207}Pb/^{206}Pb$ of 0.2108 identical within uncertainty to the measured ratio of 0.20 ± 0.02 (1σ) in Gn 1 (Fig. 8A, C). The isolation time of Pb_1^* (i.e. Pb^* formed by radioactive decay within monazite between 2440 and 1045 Ma) at *ca.* 1045 Ma is supported by the $^{208}Pb/^{232}Th$ date of 1171 ± 170 Ma (Appendix G.8) obtained by APT from the host monazite adjacent to Gn 1 in specimen M6 (Fig. 4A). Thus, we interpret that the isolation of Pb_1^* and the crystallization of galena Gn 1 occurred at t_1 = 1045 Ma.

Galena Gn 2 has a significantly different $^{207}Pb/^{206}Pb$ ratio of 0.150 ± 0.003 (1σ) that cannot be explained by a single Pb* isolation event since the present-day $^{207}Pb/^{206}Pb$ ratio of a monazite that crystallized at 2440 Ma would be 0.1585 (Fig. 8A). The possibility for Gn 2 to result from

387 a mixing of two Pb^* components is thus explored using the well-known t_0, t_1 and t_2 events. This
388 scenario involves a first Pb^* component (Pb_1^*) produced by U and Th decay between t_0 and t_1
389 with a theoretical $^{207}Pb/^{206}Pb$ isotopic signature of 0.2108, and a second Pb^* component (Pb_2^*)
390 produced by U and Th decay between t_1 and t_2 with a theoretical $^{207}Pb/^{206}Pb$ isotopic signature
391 of 0.0901. At 550 Ma, the $^{207}Pb/^{206}Pb$ ratio of 0.150 recorded by Gn 2 is then obtained by a
392 mixture of 53% Pb_2^* and 47% Pb_1^*, in a grain which underwent 70% Pb_1^* loss at t_1 with 30%
393 remaining captured by the galena (Fig. 8B, C). This 70% Pb_1^* loss fits the microscale U–Th–
394 Pb data for monazite grain 25 domains with a low density of inclusions (Fig. 6B). The
395 $^{208}Pb/^{232}Th$ date of 712 ± 121 Ma (2σ) (Appendix G.8) obtained by APT from the host monazite
396 adjacent to Gn 2 in specimen M17 (Fig. 4A) supports the formation of Gn 2 at t_2, a younger
397 event than t_1. This preferred scenario is not unique since: (1) microscale data suggests variable
398 Pb_1* loss at t_1, ranging from 10 to 90 % (Fig. 6) and (2) variable proportions of Pb_1^* and Pb_2^*
399 could be mobilized and mixed at t_2, corresponding to a theoretical range of $^{207}Pb/^{206}Pb$ isotopic
400 compositions between 0.0901 – 0.1806 for the galena (Fig. 8C). This observation cautions about
401 the interpretation of $^{207}Pb/^{206}Pb$ ratios in Pb-rich nanominerals in term of ages.

402 ## 5.4.Time-integrated model of monazite evolution

403 The theoretical evolution of U–Pb and Pb–Pb ratios in a monazite that crystalized at *ca.*
404 2440 Ma have been modelled and the results are displayed in Tera-Wasserburg diagrams along
405 with snapshots of Pb distribution in the monazite crystal over time (Fig. 8D). After monazite
406 crystallization at t_0, U and Th decay in monazite produce Pb_1^* (red spots, Fig. 8D). The APT
407 average $^{208}Pb/^{232}Th$ age of 1021 ± 263 Ma (2σ) indicates that the monazite matrix becomes
408 completely reset at the nanoscale. This resetting event corresponds to the amphibolite-facies
409 Rayner event at *ca.* 1045 Ma. This metamorphic event is recorded in our rock sample 5037 by
410 garnet retrogression into biotite and by recrystallization of (UHT) Rt-quartz in rutile-free, low-
411 Ti quartz ribbons. Clear evidence of fluid-rock interaction and plastic deformation thus exists

in the rock sample 5037 at *ca.* 1045 Ma. Lead mobility in monazite has been shown to be enhanced both by fluid present conditions (Seydoux-Guillaume et al., 2002) and deformation (Erickson et al., 2015; Fougerouse et al., 2021b) or a combination of both (Wawrzenitz et al., 2012).

In presence of reactive metamorphic fluids, experimental studies demonstrate that the resetting of monazite U–Pb and Th–Pb chronometers at the nanoscale could arise through pseudomorphic replacement with the formation of a new monazite free of Pb^* only recognizable at the nanoscale (Grand'Homme et al., 2018, 2016). Whilst the APT age of 1021 ± 263 Ma (2σ) suggests that the monazite matrix is completely reset at t_1, we cannot completely exclude that subordinate nanodomains of monazite crystallized at 2440 Ma may still be present after t_1, accounting for the dispersion and large uncertainties of the monazite matrix dates measured by APT (Appendix G.9). Compared to these experimental studies, the replacement process in this natural example is coupled with Pb-bearing nanominerals (galena) crystallization. This contrast could reflect differences in experimental versus natural rock reaction kinetics or fluid/mineral ratios, or fluid compositions. Indeed, nanopores filled with SiO_2 are frequently observed in experimental studies because a NaOH fluid saturated in Si is used. In natural monazite, the local fluid saturation in Pb might be achieved by relatively low fluid/monazite ratio typical of dry rocks like UHT granulite and a high Pb* concentration typical of old Th-rich monazite.

Following the t_1 event, Pb_2^* forms from the further decay of U and Th in the monazite (green spots, Fig. 8D). At *ca.* 550 Ma (t_2), a hydrothermal event associated with pegmatite formation triggers the crystallization of a second generation of galena (Gn 2) composed by the mixing of $Pb_1^* + Pb_2^*$. The Pb_2^* component is derived from the monazite matrix at t_2 and correspond to Pb^* growth between t_1 and t_2. Mobilization of Pb_2^* to form Gn 2 is more cryptic as it is not related to an extensive resetting of the Th–Pb chronometer in the monazite matrix compared to the first generation of galena. The monazite matrix adjacent to Gn 2 yields the youngest Th–Pb

date of 712 ± 121 Ma (2σ), which sits between t_1 and t_2. Consequently, Pb migration at t_2 occurred at a smaller scale than at t_1 and might not be completely resolved at the current scale of investigation. This is confirmed by the microscale observation that in contrast to t_1 event, the effect of the t_2 event is insufficient to cause significant Pb^* loss at the grain scale (Fig. 6). The galena 2 therefore rather witnesses intra-grain and short-range redistribution of Pb, involving a Pb_2^* and a Pb_1^* component that could be derived from either the first galena (Gn 1) or from monazite matrix in case of old nanodomains have been preserved in the matrix at t_1.

6. CONCLUSION and PERSPECTIVES

This study explores the isotopic disturbance of the U–Th–Pb systems in monazite from a UHT Archean granulite using multiple methods for characterization and dating from the micro- (LA-ICP-MS, SIMS, EMP) to the nanoscale (TEM, APT). At the microscale the dates are discordant and spread along a discordia between *ca.* 2440 and *ca.* 1045 Ma. Our observations reveal that the least discordant monazite grains are brown in color because they contain a high density of small (~ 50 nm) Pb-bearing nanominerals homogeneously distributed in the grain whereas the most discordant and optically clear monazite grains contain larger (50- 500 nm) but sparser Pb-bearing nanominerals, some of them being identified as galena (PbS) on the basis of TEM and APT observations. The discordia observed with conventional *in-situ* methods at the microscale thus reflects a mixing within the analytical volume of matrix monazite and galena. The percentage of Pb-loss is in turn linked to monazite textural position as initially observed by Black et al. (1984). Monazite shielded in UHT phases like garnet or Rt-quartz show a low percentage of Pb-loss and a high density of galena inclusions. In contrast monazite hosted in the re-equilibrated quartzo-feldspathic matrix show a high percentage of Pb-loss and lower density of galena inclusions. The retention of Pb* in galena is promoted by monazite shielding in (anhydrous) UHT phases like garnet and Rt-quartz.

The Pb isotopic compositions of the galena grains are variable but imply an *in-situ* radiogenic origin with no participation of common Pb. The $^{207}Pb/^{206}Pb$ ratios of the galena, when considered in combination with the $^{208}Pb/^{232}Th$ ages of the monazite matrix (excluding galena) measured with APT, and the constrains given by regional geology, indicate two episodes of Pb^* mobility. This study suggests that monazite crystallized at *ca.* 2440 Ma and was affected at *ca.* 1045 Ma by variable Pb^*-loss at the grain scale, characterized at the nanoscale by a resetting of the monazite matrix through pseudomorphic replacement associated with Pb^* retention as galena Gn 1 in variable proportions. A second episode of Pb^* mobility is recorded by the crystallization of a second generation of galena Gn 2 and is likely related to a younger event at *ca.* 550 Ma. Pb^* in Gn 2 galena corresponds to a mixing of Pb_1^* and Pb_2^* likely reworked from the pre-existing Gn 1 (Pb_1^*) and monazite matrix (Pb_2^*) with much more localized effect on the resetting of the monazite matrix as no date of 550 Ma was found by APT.

Combining a multi-scale characterization, this study demonstrates the importance of nanoscale structural, chemical and isotopic observations to understand microscale age disturbances by providing a new perspective on the origin of the discordance in monazite. Indeed, the retention of Pb^* in the form of Pb-bearing nanominerals within monazite grain could be a phenomenon that is, if not prevalent, at least shared by monazite crystals when certain conditions are met. These conditions may include an ancient and long-lived geological history (Archean – Proterozoic) resulting in high Pb^* content, a monazite composition having a sufficient S content to form galena and the presence of reactive fluids. However other Pb-bearing nanominerals might crystallize if S is unavailable. For example, Pb-bearing nanominerals have been found in discordant Archean UHT monazite from Madagascar (Paquette et al., 2004; Seydoux-Guillaume et al., 2003). Hence, discordance in monazite is explained by the partial loss of Pb^* through a coupled dissolution-precipitation process and the retention of the remaining Pb^* within monazite as Pb^*-bearing nanominerals (e.g. galena). In

combination with a good understanding of the regional framework and the thermal events in an area, the identification of Pb^*-bearing nanominerals can be used to understand the complexities of Pb^* migration processes in minerals. The presence of numerous Pb^*-bearing nanominerals within monazite grains therefore presents new opportunities for geochronologists to decipher the thermal history of complex metamorphic terrains.

Acknowledgments

We thank Ph. De Parseval and S. Gouy for their technical assistance with the microprobe, C. Talavera-Rodriguez for the SIMS, C. Fellah for SEM, V. Bosse and R. Dubost for the LA-ICP-MS. UJM and CNRS (INSU TelluS-SYSTER and IEA nanomobility) are thanked for financial support and CAMECA for access to Ivas software. D. Fougerouse acknowledges funding from the Australian Research Council (DE190101307). We thank Alex Webb for editorial handling and Monika Kusiak and one anonymous reviewer for providing constructive comments.

Appendices

Appendix A. Details on the methods, including sample preparation, analytical conditions, calibration and data processing

Appendix B. Complementary observations of microscale to nanoscale features including optical microscopy, scanning electron imaging, transmission electron microscopy and atom probe mass spectrum of monazite

Appendix C. U-Th-Pb SIMS dataset

Appendix D. U-Th-Pb LA-ICP-MS dataset

Appendix E. U-Th-Pb EMP dataset

Appendix F. U-Th-Pb data plotted on figure 5

Appendix G. Complementary figures of U–Th–Pb geochronology

Appendix H. Th-Pb APT dataset

References

Allègre, C.J., Albarède, F., Grünenfelder, M., Köppel, V., 1974. 238U/206Pb-235U/207Pb-232Th/208Pb Zircon Geochronology in Alpine and Non-Alpine Environment. Contributions to Mineralogy and Petrology 43, 194.

Arcuri, G.A., Moser, D.E., Reinhard, D.A., Langelier, B., Larson, D.J., 2020. Impact-triggered nanoscale Pb clustering and Pb loss domains in Archean zircon. Contributions to Mineralogy and Petrology 175, 1–13. https://doi.org/10.1007/s00410-020-01698-w

Asami, M., Suzuki, K., Grew, E.S., 2002. Chemical Th-U-total Pb dating by electron microprobe analysis of monazite, xenotime and zircon from the Archean Napier complex, East Antarctica: Evidence for ultra-high-temperature metamorphism at 2400 Ma. Precambrian Research 114, 249–275. https://doi.org/10.1016/S0301-9268(01)00228-5

Black, L.P., Fitzgerald, J.D., Harley, S.L., 1984. Pb isotopic composition, colour, and microstructure of monazites from a polymetamorphic rock in Antarctica. Contributions to Mineralogy and Petrology 85, 141–148.

Black, L.P., Harley, S.L., Sun, S.S., McCulloch, M.T., 1987. The Rayner Complex of East Antarctica: complex isotopic systematics within a Proterozoic mobile belt. Journal of Metamorphic Geology 5, 1–26. https://doi.org/10.1111/j.1525-1314.1987.tb00366.x

Black, L.P., James, P.R., Harley, S.L., 1983. Geochronology and geological evolution of metamorphic rocks in the Field Islands area, East Antarctica. Journal of Metamorphic Geology 1, 277–303. https://doi.org/10.1111/j.1525-1314.1983.tb00276.x

Blum, T.B., Reinhard, D.A., Chen, Y., Prosa, T.J., Larson, D.J., Valley, J.W., 2018. Uncertainty and sensitivity analysis for spatial and spectral processing of Pb isotopes in zircon by atom probe tomography. Geophysical Monograph Series 232, 327–350. https://doi.org/10.1002/9781119227250.ch16

Broom-Fendley, S., Smith, M.P., Andrade, M.B., Ray, S., Banks, D.A., Loye, E., Atencio, D., Pickles, J.R., Wall, F., 2020. Sulfur-bearing monazite-(Ce) from the Eureka carbonatite, Namibia: oxidation state, substitution mechanism, and formation conditions. Mineralogical Magazine 84, 35–48. https://doi.org/10.1180/mgm.2019.79

Cappelli, C., Pérez-Huerta, A., 2020. Effect of crystallographic orientation on atom probe tomography geochemical data? Micron 137, 102910. https://doi.org/10.1016/j.micron.2020.102910

Carson, C.J., Ague, J.J., Grove, M., Coath, C.D., Harrison, T.M., 2002. U-Pb isotopic behaviour of zircon during upper-amphibolite facies fluid infiltration in the Napier Complex, East Antarctica. Earth and Planetary Science Letters 199, 287–310. https://doi.org/10.1016/S0012-821X(02)00565-4

Chakhmouradian, A.R., Mitchell, R.H., 1999. Niobian ilmenite, hydroxylapatite and sulfatian alternative hosts for incompatible in calcite elements. Canadian Mineralogist 37, 1177–1189.

Corfu, F., 2013. A century of U-pb geochronology: The long quest towards concordance. Bulletin of the Geological Society of America 125, 33–47. https://doi.org/10.1130/B30698.1

Erickson, T.M., Pearce, M.A., Taylor, R.J.M., Timms, N.E., Clark, C., Reddy, S.M., Buick, I.S., 2015. Deformed monazite yields high-temperature tectonic ages. Geology 43, 383–386. https://doi.org/10.1130/G36533.1

555 Fougerouse, D., Cavosie, A.J., Erickson, T., Reddy, S.M., Cox, M.A., Saxey, D.W., Rickard,
556 W.D.A., Wingate, M.T.D., 2021a. A new method for dating impact events – Thermal
557 dependency on nanoscale Pb mobility in monazite shock twins. Geochimica et
558 Cosmochimica Acta 314, 381–396. https://doi.org/10.1016/j.gca.2021.08.025

559 Fougerouse, D., Kirkland, C., Saxey, D., Seydoux-Guilllaume, A.M., Rowles, M.R., Rickard,
560 W.D.A., Reddy, S.M., 2020. Nanoscale isotopic dating of monazite. Geostandards and
561 Geoanalytical Research in press. https://doi.org/10.1111/ggr.12340

562 Fougerouse, D., Reddy, S.M., Saxey, D.W., Erickson, T., Kirkland, C.L., Rickard, W.D.A.,
563 Seydoux-Guillaume, A.M., Clark, C., Buick, I.S., 2018. Nanoscale distribution of Pb in
564 monazite revealed by atom probe microscopy. Chemical Geology 479, 251–258.
565 https://doi.org/10.1016/j.chemgeo.2018.01.020

566 Fougerouse, D., Reddy, S.M., Seydoux-Guillaume, A., Kirkland, C.L., Erickson, T.M.,
567 Saxey, D.W., Rickard, W.D.A., Jacob, D., Clark, C., 2021b. Mechanical twinning of
568 monazite expels radiogenic lead. Geology 49, 417–421.
569 https://doi.org/https://doi.org/10.1130/G48400.1

570 Fougerouse, D., Saxey, D., Rickard, W., Reddy, S., Verberne, R., 2021c. Standardizing
571 Spatial Reconstruction Parameters for the Atom Probe Analysis of Common Minerals.
572 Microscopy and Microanalysis 1–10. https://doi.org/10.1017/S1431927621013714

573 Gebauer, D., Grünenfelder, M., 1979. U-Th-Pb Dating of Minerals, in: Jäger, E., Hunziker,
574 J.C. (Eds.), Lectures in Isotopic Geology. Berlin Heidelberg New York, pp. 105–131.
575 https://doi.org/10.1007/978-3-642-67161-6

576 Grand'Homme, A., Janots, E., Seydoux-Guillaume, A.M., Guillaume, D., Bosse, V., Magnin,
577 V., 2016. Partial resetting of the U-Th-Pb systems in experimentally altered monazite:
578 Nanoscale evidence of incomplete replacement. Geology 44, 4–7.

https://doi.org/10.1130/G37770.1

Grand'Homme, A., Janots, E., Seydoux-Guillaume, A.M., Guillaume, D., Magnin, V., Hövelmann, J., Höschen, C., Boiron, M.C., 2018. Mass transport and fractionation during monazite alteration by anisotropic replacement. Chemical Geology 484, 51–68. https://doi.org/10.1016/j.chemgeo.2017.10.008

Harley, L., Hensen, B.J., 1990. Archean and Proterozoic high grade terranes of East Antarctica (40-80°E): a case study of diversity in granulite facies metamorphism. In: Ashworth, J. R. & Brown, M. (eds) High-temperature Metamorphism and Crustal Anatexis. Unwin Hyman, London, 320-370

Harley, S.L., 2003. Archaean-Cambrian crustal development of East Antarctica: metamorphic characteristics and tectonic implications. Geological Society, London, Special Publications 206, 203–230. https://doi.org/10.1144/gsl.sp.2003.206.01.11

Harley, S.L., Kelly, N.M., Kusiak, M.A., 2019. Ancient Antarctica : The Archean of the East Antarctic Shield. Earth's Oldest Rocks 865–897.

Harley, S.L., Motoyoshi, Y., 2000. Al zoning in orthopyroxene in a sapphirine quartzite: Evidence for >1120 °C UHT metamorphism in the Napier Complex, Antarctica, and implications for the entropy of sapphirine. Contributions to Mineralogy and Petrology 138, 293–307. https://doi.org/10.1007/s004100050564

Hokada, T., Misawa, K., Yokoyama, K., Shiraishi, K., Yamaguchi, A., 2004. SHRIMP and electron micropobe chronology of UHT metamorphism in the Napier Complex, East Antarctica: Implications for zircon growth at >1,000 °C. Contributions to Mineralogy and Petrology 147, 1–20. https://doi.org/10.1007/s00410-003-0550-2

Kelly, N.M., Harley, S.L., 2005. An integrated microtextural and chemical approach to zircon

602 geochronology: Refining the Archaean history of the Napier Complex, east Antarctica.
603 Contributions to Mineralogy and Petrology 149, 57–84. https://doi.org/10.1007/s00410-
604 004-0635-6

605 Krenn, E., Putz, H., Finger, F., Paar, W.H., 2011. Sulfur-rich monazite with high common Pb
606 in ore-bearing schists from the Schellgaden mining district (Tauern Window, Eastern
607 Alps). Mineralogy and Petrology 102, 51–62. https://doi.org/10.1007/s00710-011-0170-
608 x

609 Kusiak, M.A., Dunkley, D.J., Wirth, R., Whitehouse, M.J., Wilde, S.A., Marquardt, K., 2015.
610 Metallic lead nanospheres discovered in ancient zircons. Proceedings of the National
611 Academy of Sciences 112, 4958–4963. https://doi.org/10.1073/pnas.1415264112

612 Kusiak, M.A., Kovaleva, E., Wirth, R., Klötzli, U., Dunkley, D.J., Yi, K., Lee, S., 2019. Lead
613 oxide nanospheres in seismically deformed zircon grains. Geochimica et Cosmochimica
614 Acta. https://doi.org/10.1016/j.gca.2019.07.026

615 Laurent, A.T., Seydoux-Guillaume, A.M., Duchene, S., Bingen, B., Bosse, V., Datas, L.,
616 2016. Sulphate incorporation in monazite lattice and dating the cycle of sulphur in
617 metamorphic belts. Contributions to Mineralogy and Petrology 171.
618 https://doi.org/10.1007/s00410-016-1301-5

619 Paquette, J.L., Goncalves, P., Devouard, B., Nicollet, C., 2004. Micro-drilling ID-TIMS U-Pb
620 dating of single monazites: A new method to unravel complex poly-metamorphic
621 evolutions. Application to the UHT granulites of Andriamena (North-Central
622 Madagascar). Contributions to Mineralogy and Petrology 147, 110–122.
623 https://doi.org/10.1007/s00410-003-0549-8

624 Peterman, E.M., Reddy, S.M., Saxey, D.W., Fougerouse, D., Quadir, M.Z., Jercinovic, M.J.,
625 2021. Trace-element segregation to dislocation loops in experimentally heated zircon.

American Mineralogist 106, 1971–1979. https://doi.org/10.2138/am-2021-7654

Peterman, E.M., Reddy, S.M., Saxey, D.W., Snoeyenbos, D.R., Rickard, W.D.A., Fougerouse, D., Kylander-Clark, A.R.C., 2016. Nanogeochronology of discordant zircon measured by atom probe microscopy of Pb-enriched dislocation loops. Science Advances 2. https://doi.org/10.1126/sciadv.1601318

Pršek, J., Ondrejka, M., Bačík, P., Budzyń, B., Uher, P., 2010. Metamorphic-hydrothermal ree minerals in the Bacúch magnetite deposit, western carpathians, Slovakia: (Sr,S)-Rich monazite-(Ce) and Nd-dominant hingganite. Canadian Mineralogist 48, 81–94. https://doi.org/10.3749/canmin.48.1.81

Seydoux-Guillaume, A.M., Fougerouse, D., Laurent, A.T., Gardés, E., Reddy, S.M., Saxey, D.W., 2019. Nanoscale resetting of the Th/Pb system in an isotopically-closed monazite grain: A combined atom probe and transmission electron microscopy study. Geoscience Frontiers. https://doi.org/10.1016/j.gsf.2018.09.004

Seydoux-Guillaume, A.M., Goncalves, P., Wirth, R., Deutsch, A., 2003. Transmission electron microscope study of polyphase and discordant monazites: Site-specific specimen preparation using the focused ion beam technique. Geology 31, 973–976. https://doi.org/10.1130/G19582.1

Seydoux-Guillaume, A.M., Paquette, J.L., Wiedenbeck, M., Montel, J.M., Heinrich, W., 2002. Experimental resetting of the U-Th-Pb systems in monazite. Chemical Geology 191, 165–181. https://doi.org/10.1016/S0009-2541(02)00155-9

Seydoux-Guillaume, A.M., Bingen, B., Bosse, V., Janots, E., Laurent, A.T., 2018a. Transmission Electron Microscope Imaging Sharpens Geochronological Interpretation of Zircon and Monazite. Microstructural Geochronology 1360, 1357–1360.

649 Seydoux-Guillaume, A.M., Deschanels, X., Baumier, C., Neumeier, S., Weber, W.J., Peuget,
650 S., 2018b. Why natural monazite never becomes amorphous: Experimental evidence for
651 alpha self-healing. American Mineralogist: Journal of Earth and Planetary Materials,
652 103(5), 824-827.

653 Suzuki, K., Kato, T., 2008. CHIME dating of monazite, xenotime, zircon and polycrase:
654 Protocol, pitfalls and chemical criterion of possibly discordant age data. Gondwana
655 Research 14, 569–586. https://doi.org/10.1016/j.gr.2008.01.005

656 Taylor, R.J.M., Clark, C., Harley, S.L., Kylander-Clark, A.R.C., Hacker, B.R., Kinny, P.D.,
657 2017. Interpreting granulite facies events through rare earth element partitioning arrays.
658 Journal of Metamorphic Geology 35, 759–775. https://doi.org/10.1111/jmg.12254

659 Tera, F., Wasserburg, G.J., 1972. U-Th-Pb systematics in three Appolo 14 basalts and the
660 problem of initial Pb in lunar rocks. Earth and Planetary Science Letters 14, 281–304.

661 Valley, J.W., Cavosie, A.J., Ushikubo, T., Reinhard, D.A., Lawrence, D.F., Larson, D.J.,
662 Clifton, P.H., Kelly, T.F., Wilde, S.A., Moser, D.E., Spicuzza, M.J., 2014. Hadean age
663 for a post-magma-ocean zircon confirmed by atom-probe tomography. Nature
664 Geoscience 7, 219–223. https://doi.org/10.1038/ngeo2075

665 Valley, J.W., Reinhard, D.A., Ushikubo, T., Snoeyenbos, D.R., Larson, D.J., Strickland, A.,
666 Cavosie, A.J., Kelly, T.F., Lawrence, D.F., 2015. Nano- and micro-geochronology in
667 Hadean and Archean zircons by atom-probe tomography and SIMS: New tools for old
668 minerals. American Mineralogist 100, 1355–1377. https://doi.org/10.2138/am-2015-
669 5134

670 Verberne, R., Reddy, S.M., Saxey, D.W., Fougerouse, D., Rickard, W.D.A., Plavsa, D.,
671 Agangi, A., Kylander-Clark, A.R.C., 2020. The geochemical and geochronological
672 implications of nanoscale trace-element clusters in rutile. Geology XX, 1–5.

https://doi.org/10.1130/g48017.1

Wawrzenitz, N., Krohe, A., Rhede, D., Romer, R.L., 2012. Dating rock deformation with monazite: The impact of dissolution precipitation creep. Lithos 134–135, 52–74. https://doi.org/10.1016/j.lithos.2011.11.025

Wendt, I., Carl, C., 1991. The statistical distribution of the mean squared weighted deviation. Chemical Geology: Isotope Geoscience Section 86, 275–285. https://doi.org/10.1016/0168-9622(91)90010-T

Wetherill, G.W., 1963. Discordant Uranium-Lead Ages II Discordant ages resulting from diffusion of Lead and Uranium. Journal of Geophysical Research 68, 2957–2965.

Whitehouse, M.J., Kusiak, M.A., Wirth, R., Ravindra Kumar, G.R., 2017. Metallic Pb nanospheres in ultra-high temperature metamorphosed zircon from southern India. Mineralogy and Petrology 111, 467–474. https://doi.org/10.1007/s00710-017-0523-1

Figures and captions

1.5-column fitting image Figure 1. Location map of the sampling area (~ 67°22’30” S and 49°03’45”E) and previous geochronological results. A, B: map location of Zircon Point in the Napier Complex, showing the UHT zone (green dotted line) and the assumed limit between the Napier and the Rayner complex (black dotted line) from Harley et al. (2019). C: Previous U–Pb geochronological result on monazite measured by ID-TIMS (multi grain) from Black et al. (1984). White diamonds along the discordia represent the percentage of Pb loss. Analytical uncertainties are lower than the size of the symbols.

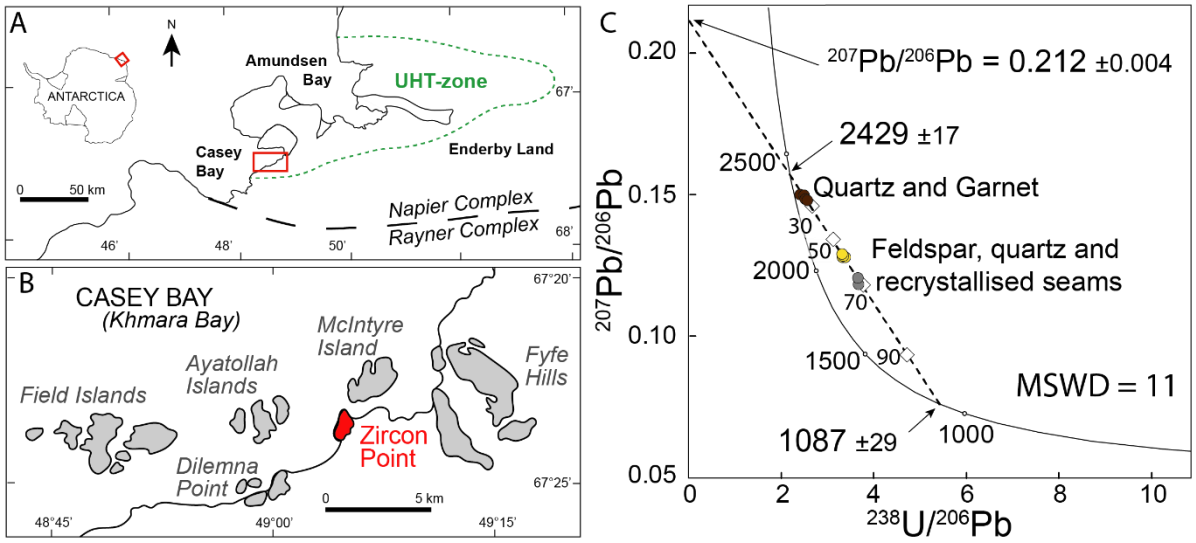

2-column fitting image Figure 2. Microscale characterization of monazite. A, B, C: High-contrast BSE SEM imaging of grains Mnz17 (A) hosted in Rt-quartz, Mnz25 (B) and Mnz2 (C) hosted in the quartzo-feldspathic matrix showing a core - rim texture along with NE-SW oriented bright (high-BSE contrast) linear features traversing the core of Mnz25 (B). The location of SIMS (white-dashed ellipses), LA-ICP-MS (full white circle) and EMP (white square) analytical spots are shown (A-C). D-F: High-contrast BSE SEM imaging of selected region of interest (red rectangles in A and B) displaying bright (high-BSE contrast) and dark (low-BSE contrast) circular inclusions. Note the smaller size of inclusions in Rt-quartz hosted monazite (D) compared to quartzo-feldspathic matrix hosted monazite (E-F) as well as the core-rim feature in (E) with inclusion-poor core and inclusion-rich rim. The location of TEM-FIB foils (A, B) and APT tips (A, C, F) are also shown with an inset showing the real size of APT site of interest (F).

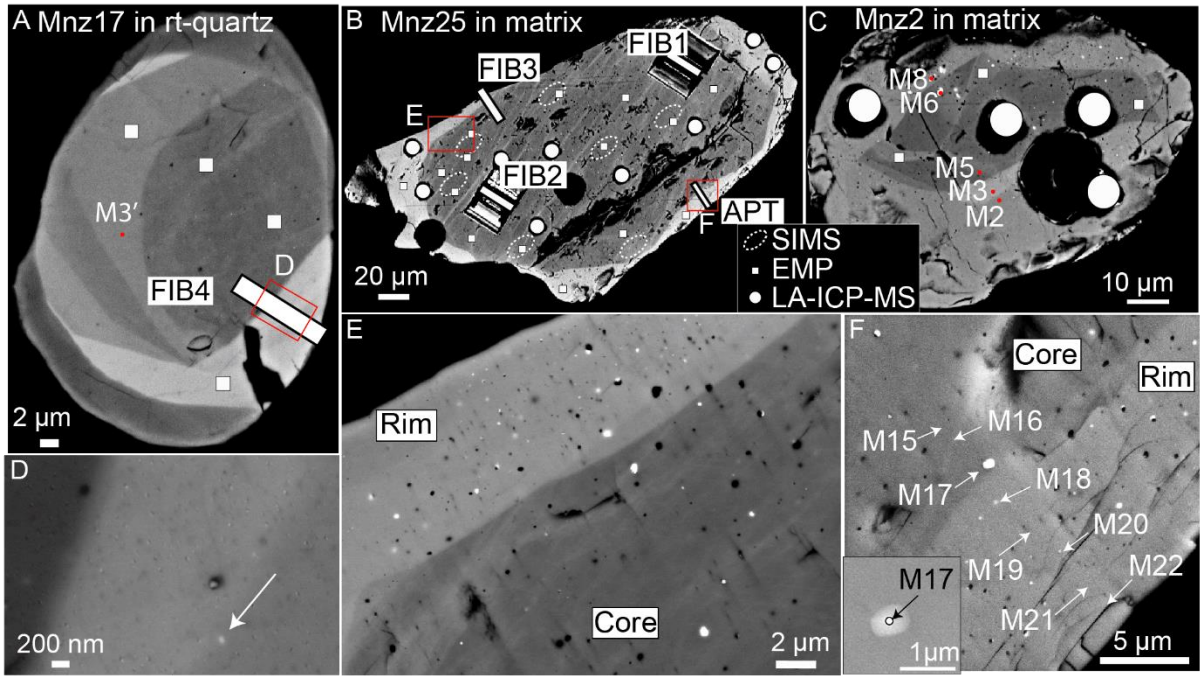

2-column fitting image Figure 3. Scanning transmission electron microscopy annular dark field images (STEM-ADF) with the same field of view for garnet hosted monazite (A) and quartzo-feldspathic matrix hosted monazite (B, C). Light grey inclusions correspond to distinct crystalline Pb-bearing minerals often polyphased and spatially associated with a dark amorphous Si-rich part. Quartzo-feldspathic matrix hosted monazite display a lower density and larger (Ø > 50 nm) light Pb-bearing minerals compared to garnet hosted monazite. Note that within quartzo-feldspathic matrix hosted monazite Mnz25, the rim (B) display a higher density of Pb-bearing minerals than the core (C). Vertical dark bands in B correspond to artefacts from FIB polishing (curtaining effects).

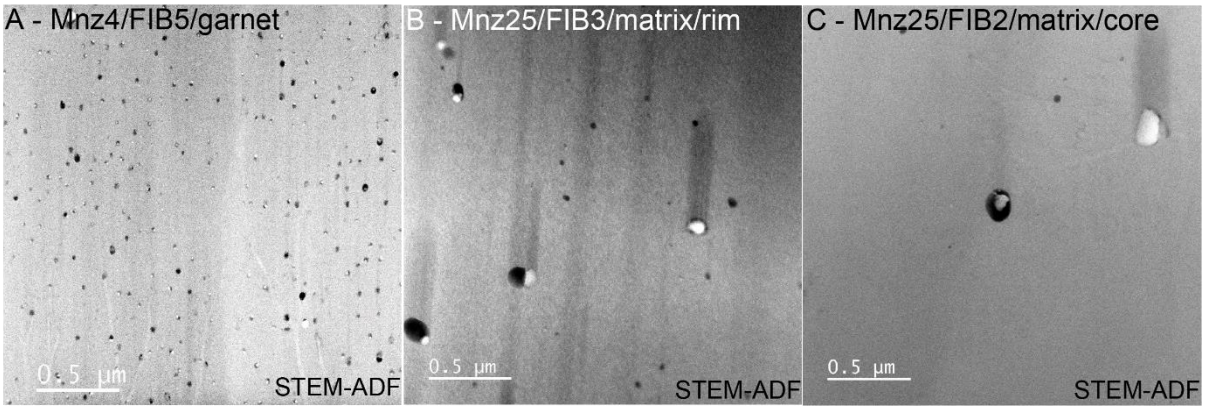

1.5-column fitting image Figure 4. APT reconstructions of M6 (from Mnz2) and M17 (from Mnz25) specimens showing S, Pb, Ce and Th atomic distribution (A). Pb and S are concentrated at the top of the tips and define galena while Pb, Ce and Th are concentrated at the bottom, highlighting the interface with monazite. $^{207}Pb/^{206}Pb$ ratios were calculated for each of the galena (errors are 1σ uncertainty) and $^{208}Pb/^{232}Th$ dates for the monazite (errors are 2σ uncertainty). B: Representative mass spectrum of galena acquired from Gn 1. Peaks are colored by molecular ions and element species. The main peaks are in good agreement with galena peaks from Cappelli and Pérez-Huerta (2020). C: Mass spectrum showing mass peaks and overlaps for Pb^{2+}. Scale bar = 100 nm. Tips locations are shown on Fig. 2C, F.

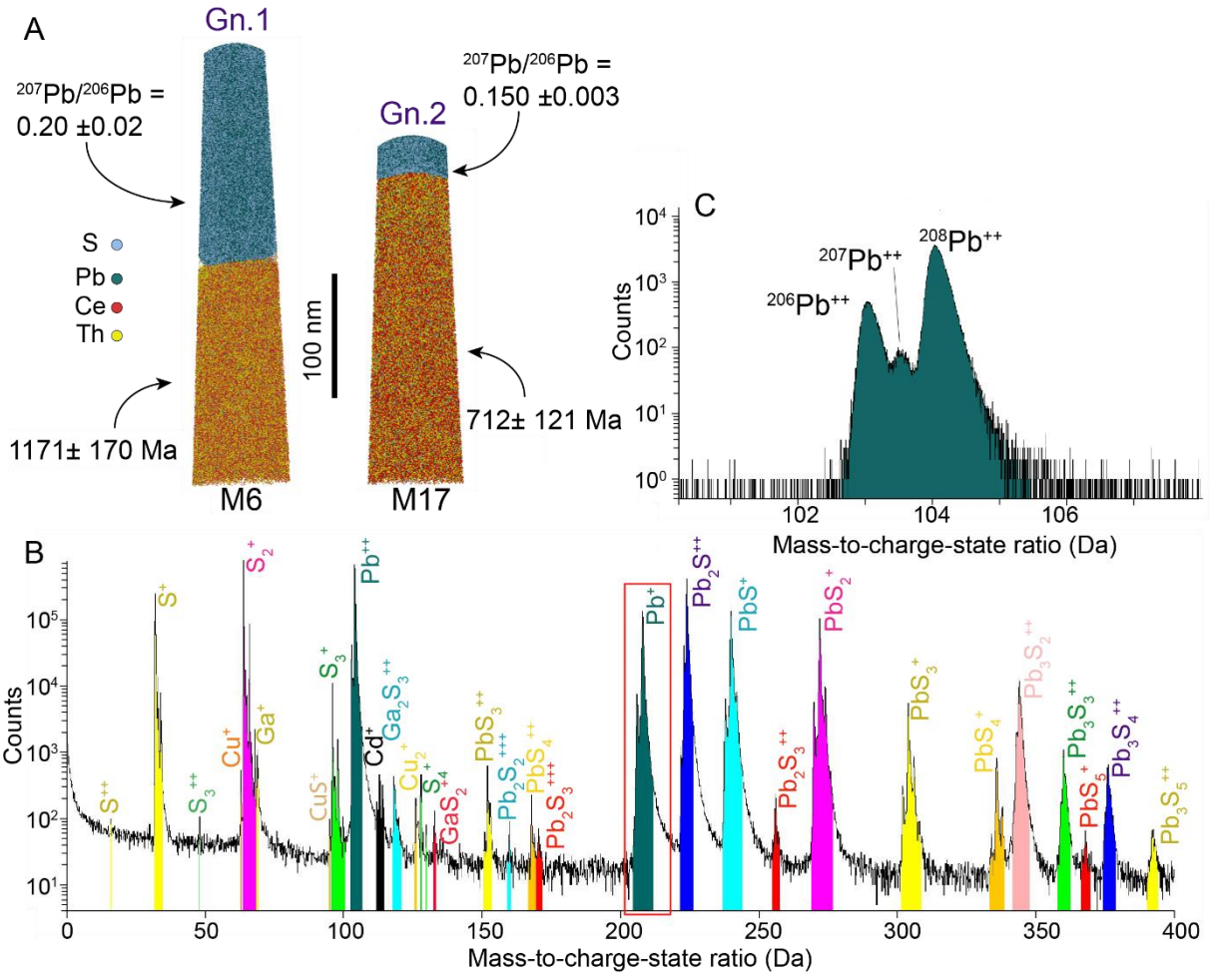

741

742

743

1.5-column fitting image Figure 5. Range of dates depending on the analytical volume. Boxplots of dates discriminated by the analytical volume referring to the technique used (ID-TIMS on multi grain from Black et al., 1984, *in-situ* LA-ICP-MS ~ 950 µm^3, SIMS ~ 600 µm^3, EMP ~ 5 µm^3 and APT < 0.008 nm^3 – this study), the analyzed domain (entire grain, core or rim), and the textural position of the analyzed grain (quartzo-feldspathic matrix = matrix, Rt-quartz, garnet or sillimanite).

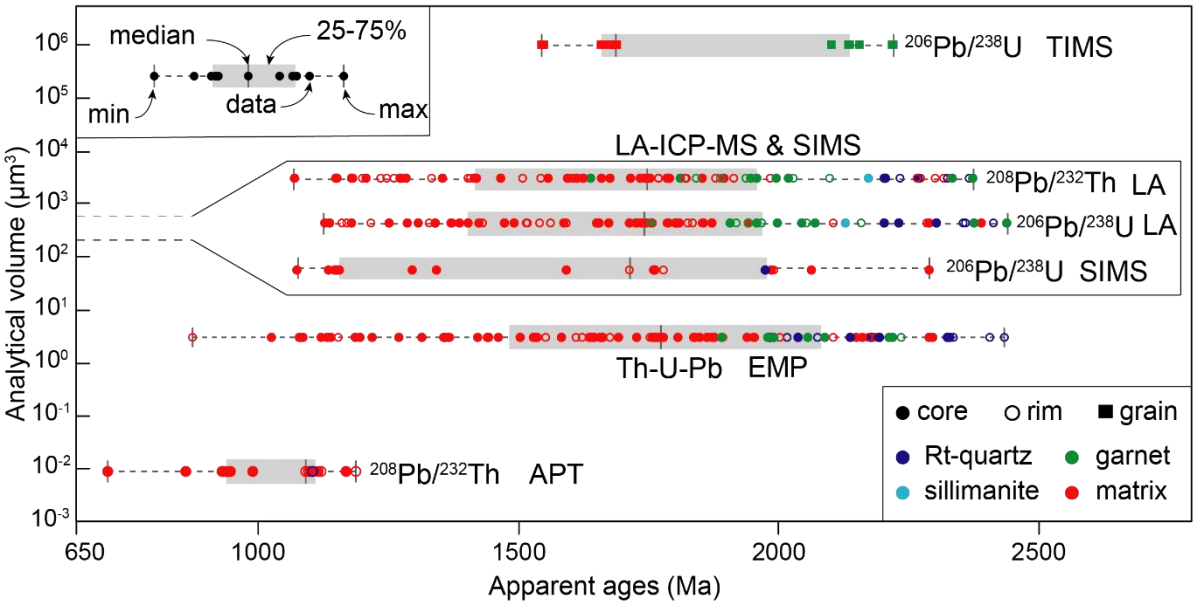

1-column fitting image Figure 6. Tera-Wasserburg diagram from LA-ICP-MS (ellipses) and SIMS (crosses) U–Pb data denoting 2σ uncertainties. White diamonds along the discordia lines represent the percentage of Pb loss. A: U–Pb data with the full dataset color-coded by host mineral. The discordia line D_{all} (solid) constructed with all data defines an upper intercept of 2383 ± 36 Ma and a lower intercept of 931 ± 45 Ma (MSWD = 4.7). Discordia constructed with data from included monazite in Rt-quartz and garnet, D_{IM} (dashed) lead to an upper intercept of 2440 ± 39 Ma and a lower intercept of 1045 ± 132 Ma (MSWD = 0.84). B: U–Pb data for selected quartzo-feldspathic matrix hosted monazite grains discriminated by the content of galena in the analyzed area. Discordia D_{LI} (solid) is constructed from the galena-rich rim domain analyses and indicate a MSWD = 2, an upper intercept of 2434 ± 181 Ma and a lower intercept of 1049 ± 248 Ma. The isotopic composition of Pb produced in the 2434–1049 Ma time interval is given by the intercept of the $^{207}Pb/^{206}Pb$ axis at 0.21 ± 0.03 (2σ). Discordia D_{FI} (large dashed) constructed from the galena-poor core domain analyses indicates a MSWD = 2.6, an upper intercept of 2120 ± 207 Ma, a lower intercept of 631 ± 224 Ma and intercepts the $^{207}Pb/^{206}Pb$ axe at 0.16 ± 0.03 (2σ). By fixing the upper intercept (discordia D_{fix}, small dashed) at 2440 Ma, the lower intercept yields a date of 861 ± 58 Ma (MSWD = 4). The purple boxes are the $^{207}Pb/^{206}Pb$ ratios, including the 1σ error, calculated for Gn 1 in M6 and Gn 2 in M17.

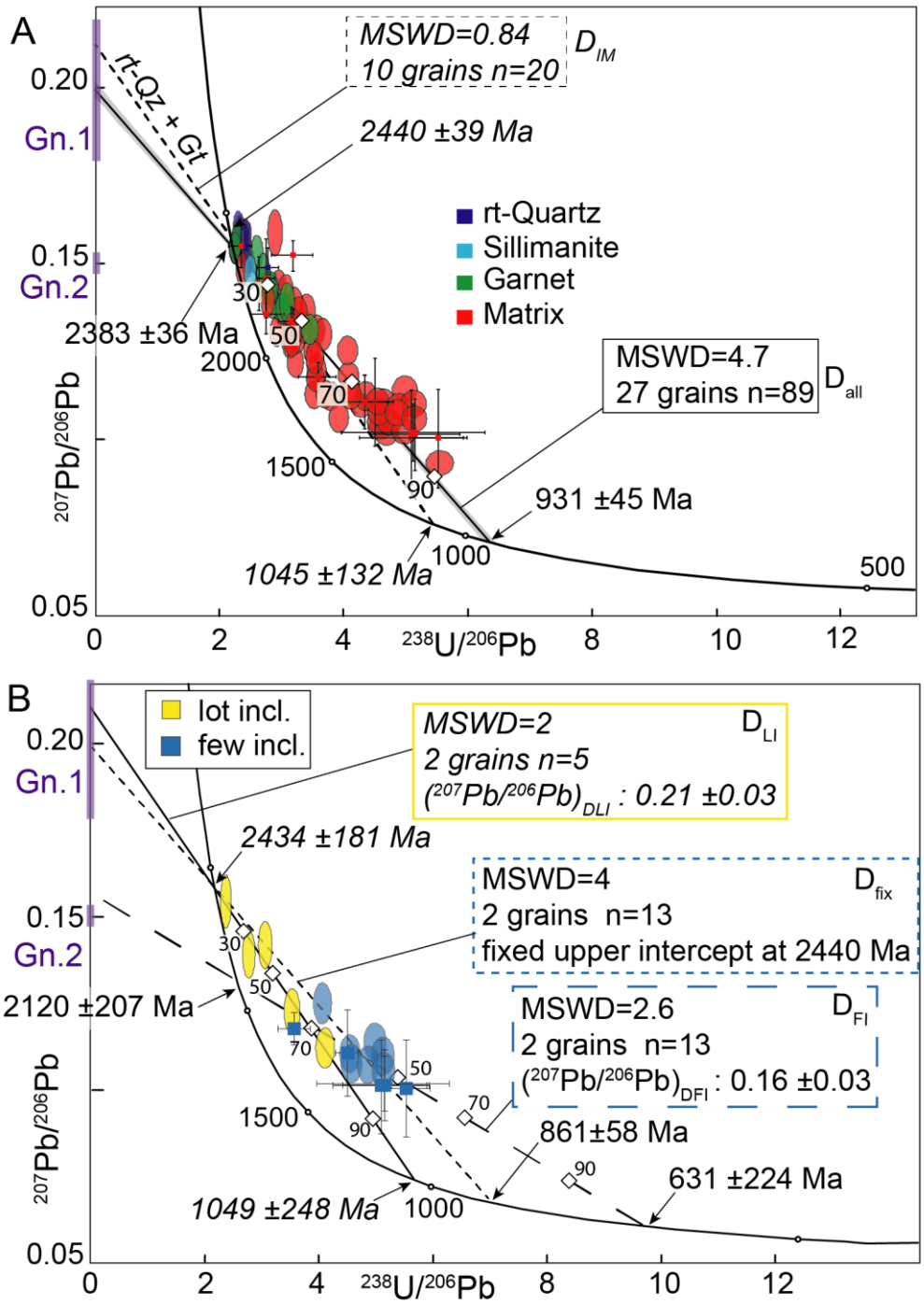
A
0.20
Gn.1
0.15
Gn.2
0.05
rt-Qz + Gt
MSWD=0.84
10 grains n=20
D_IM
2440 ±39 Ma
rt-Quartz
Sillimanite
Garnet
Matrix
2383 ±36 Ma
2000
30
50
70
90
1500
1000
500
MSWD=4.7
27 grains n=89
D_all
931 ±45 Ma
1045 ±132 Ma
207Pb/206Pb
238U/206Pb
0
2
4
8
10
12
B
lot incl.
few incl.
MSWD=2
2 grains n=5
(207Pb/206Pb)DLI : 0.21 ±0.03
D_LI
2434 ±181 Ma
MSWD=4
2 grains n=13
fixed upper intercept at 2440 Ma
D_fix
MSWD=2.6
2 grains n=13
(207Pb/206Pb)DFI : 0.16 ±0.03
D_FI
2120 ±207 Ma
861±58 Ma
631 ±224 Ma
1049 ±248 Ma

1-column fitting image Figure 7. APT reconstructions of quartzo-feldspathic matrix hosted monazite Mnz25 and Mnz2 in core (M16, M15, M5) and rim (M19) showing Ce and Th atomic distribution. One dot represents one atom. Scale bar = 100 nm. Tips locations are shown on Fig. 2C, F.

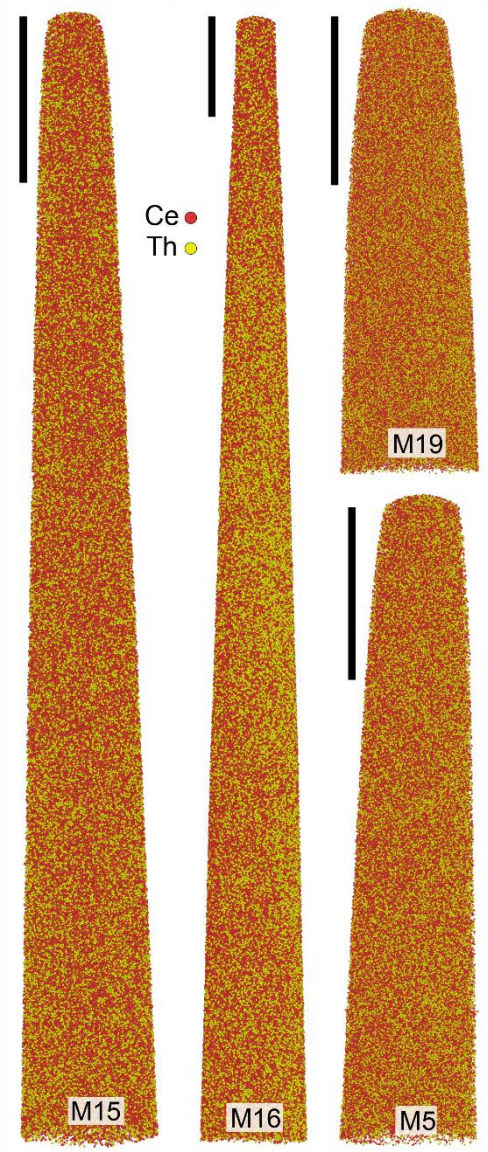

1.5-column fitting image Figure 8. A: Theoretical $^{207}Pb/^{206}Pb$ evolution in a monazite crystallized at 2440 Ma and showing the theoretical value of an isolated reservoir (i.e. galena) formed at 1045 Ma correlating with $^{207}Pb/^{206}Pb$ of Gn 1 within error limits (purple box). B: Theoretical Pb_1^* component proportion required to form a $^{207}Pb/^{206}Pb$ signature of 0.150 considering a Pb_1^* + Pb_2^* mixing over time in the studied monazite. C: Theoretical evolution of $^{238}U/^{206}Pb$ and $^{207}Pb/^{206}Pb$ ratio in a Tera-Wasserburg diagram for a monazite which crystallizes at 2440 Ma (t_0) and undergoes two events of Pb^* mobility at 1045 Ma (t_1) and 550 Ma (t_2). D: Schematic Pb^* mobility in monazite; t_0 monazite crystallization free of Pb^*, t_0 to t_1 Pb_1^* growth (red spots), at t_1 x% of Pb_1^* loss at the grain scale along with resetting of monazite matrix and 1-x% of Pb_1^* isolation as galena. Then t_1 to t_2 Pb_2^* growth in monazite matrix (green spots). At t_2 Pb^* mixing and isolation as galena in variable proportion of Pb_1^* and $Pb_2^*$and t_{actual} theoretical state of the monazite grain.